Escape time statistics for mushroom billiards

Tomoshige Miyaguchi[1,*]
[1]*Meme Media Laboratory, Hokkaido University, Kita-Ku, Sapporo 060-0813, Japan*
(Received 15 February 2007; published 27 June 2007)

Chaotic orbits of the mushroom billiards display intermittent behaviors. We investigate statistical properties of this system by constructing an infinite partition on the chaotic part of a Poincaré surface, which illustrates details of chaotic dynamics. Each piece of the infinite partition has a unique escape time from the half disk region, and from this result it is shown that, for fixed values of the system parameters, the escape time distribution obeys a power law $1/t_{\mathrm{esc}}^3$.

DOI: 10.1103/PhysRevE.75.066215 PACS number(s): 05.45.−a

I. INTRODUCTION

Fully chaotic dynamical systems such as the Baker transformation and the Arnold's cat map are statistically characterized by, for example, exponential decay of correlation functions with decay rates given by the Pollicotte-Ruelle resonances (see Ref. [1], and references therein) and exponentially fast escapes from regions of phase spaces with the escape rate given by the positive Lyapunov exponents and the Kolmogolov-Sinai (KS) entropy [2,3]. These properties are outcomes of uniform hyperbolicity, which means the uniform instability of chaotic trajectories.

In contrast to such ideally chaotic systems, phase spaces of generic Hamiltonian systems consist not only of nonintegrable chaotic regions but also of integrable regions (regions filled with tori), where motions are quasiperiodic [4], and therefore the uniform instability does not hold for these systems. In fact, generic Hamiltonian systems frequently exhibit power law type behaviors, that are due to occasional trappings of chaotic orbits in neighborhoods of torus regions. Although these phenomena are observed in many systems [5–9], analytical derivations of decaying properties of correlation functions and escape time distributions are difficult mainly because there exist complex fractal torus structures.

In order to understand power law behaviors in dynamical systems, nonhyperbolic one-dimensional mappings have been studied by several authors (e.g., Refs. [10–14]) and they have found power law behaviors in their models. Therefore it is natural to imagine a close connection between these nonhyperbolic maps and mixed type Hamiltonian systems, however, extensions of these maps to two-dimensional area-preserving systems are unknown (but see Refs. [15,16]). Thus it is important to elucidate the typical properties of nonhyperbolicity in the mixed type Hamiltonian systems.

The mushroom billiard, which has been proposed by Bunimovich recently [17], is expected to be a candidate of analytically tractable model for such problems of mixed type systems. This is because the mushroom billiard system does not have the fractal torus structures and chaotic and torus regions are sharply divided (see Ref. [18] for another example of such systems). Thus the mushroom billiard system can be thought as an ideal model for understanding mixed type Hamiltonian systems, and it is currently under active study [19–23]. An understanding of the classical system should be important for the study of the quantum version of the mushroom billiard.

Escape time statistics are important for various applications, e.g., chemical reactions [24,25], chaotic ionization [26], and fluid dynamics [27]. In these studies, the escape from a potential well over saddle points was investigated, while, in this paper, we focus on the statistical properties of the escape from neighborhoods of torus regions and there is no saddle point. We show a theoretical derivation of the escape time distribution for the mushroom billiard for fixed values of the system parameters. In Refs. [20,21], it has already been shown that it obeys power law by numerical simulations and a heuristic analysis. It is shown that our analytical result agrees with theirs perfectly. In order to derive the escape time distribution, we begin with a construction of an infinite partition on a Poincaré surface, which also reveals detailed dynamics in neighborhoods of the outermost tori.

This paper is organized as follows. In Sec. II, we introduce the mushroom billiard system, and define a Poincaré map and its inverse transformation. In Sec. III, we construct the infinite partition by using the inverse of the Poincaré map recursively. In Sec. IV, the escape time distribution is derived from the structure of the infinite partition. A brief discussion is given in Sec. V.

II. POINCARÉ MAP AND ITS INVERSE

The mushroom billiard is defined by the motion of a point particle on the billiard table depicted in Fig. 1. This table consists of a half disk (the cap) of radius R and a rectangle (the stem) of width r and height h [17]. We use the polar coordinates (u,θ), and the Cartesian coordinates (x,y); we set the origin at the center of the half disk in both cases. The angle variable θ is defined as the angle between the position vector of the point particle and the vertical axis (see Fig. 1).

A. The definition of the Poincaré map

We define a Poincaré surface at the top arc of the cap $x^2+y^2=R^2(y\geqslant 0)$ with negative momentum in the radial direction, namely, just after the collision with the arc. For the coordinates of the Poincaré map, we use the angle θ and the

*tomo@nse.es.hokudai.ac.jp

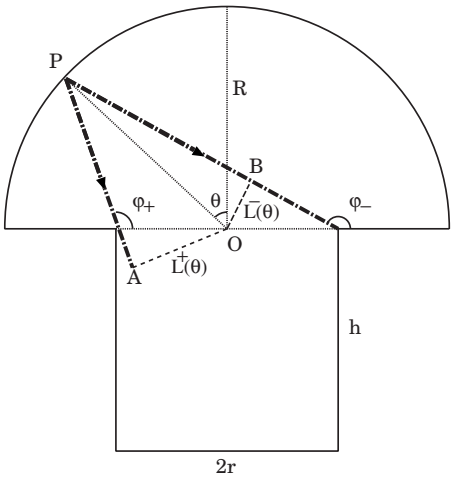

FIG. 1. The shape of the table of the mushroom billiard (the solid lines), which consists of a half disk (the cap) and a rectangle (the stem). A point particle inside the table moves freely except for the elastic collisions with the walls. The absolute value of the angular momentum $|L|$ equals the distance between the origin and the trajectory (see Sec. II A). The boundaries $L^{\pm}(\theta)$ of the first escape domain $L^{-}(\theta)<L<L^{+}(\theta)$ are also displayed (see Sec. II B).

associated angular momentum L. This Poincaré map $\Phi(L,\theta)$ is area preserving; it can be proved through a direct calculation of the Jacobian of the map which is equal to 1 everywhere. This coordinate system is slightly different from the Birkhoff coordinates, because the former is defined only on the arc, but the latter on the whole boundary of the billiard table.

We also set the kinetic energy as $v_x^2+v_y^2=1$. Although this setting is not essential, it is convenient for calculating the angular momentum $L=\boldsymbol{r}\times\boldsymbol{v}$; the absolute value of the angular momentum $|L|$ equals the distance from the origin to the trajectory. In Fig. 1, for example, if a point particle moves on the line PA in the direction indicated in the figure by the arrow, its angular momentum L $(L>0)$ equals the length of the segment AO (the dashed line), and if a point particle moves on the line PB in the direction indicated in the figure by the arrow, the absolute value of the angular momentum $-L$ $(L<0)$ equals the length of the segment BO (the long-dashed line).

We display an example of the Poincaré surface in Fig. 2. The Poincaré map $\Phi(L,\theta)$ is defined on

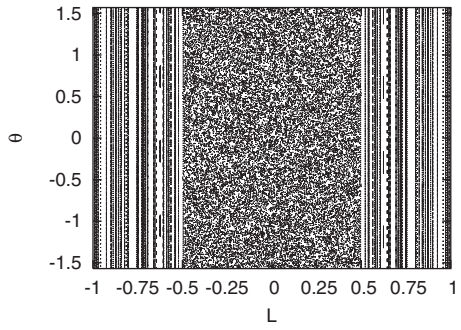

FIG. 2. The Poincaré surface for $R=1$, $r=0.5$, and $h=1$. The region $|L|<0.5$ is chaotic and the other integrable.

$$\mathcal{D}=\{(L,\theta)\in[-R,R]\times[-\pi/2,\pi/2]\};$$

the region $|L|<r$ is chaotic, and $|L|>r$ is filled with torus. The Poincaré map is symmetric with respect to the origin $(L,\theta)=(0,0)$, i.e., $\Phi(L,\theta)=-\Phi(-L,-\theta)$. In the subsequent subsections, we will restrict the domain of the Poincaré map to the region of the negative angular momentum in order to simplify the analysis.

B. The first escape and injection domains

Let us consider a point (L,θ) on the Poincaré surface such that the orbit of the billiard system (the continuous time flow) starting from this point escapes from the cap region to the stem without collision. We define the first escape domain $\mathcal{D}_1$ as all such points on the Poincaré surface. The boundary of $\mathcal{D}_1$ can be calculated analytically as follows. Let us fix the angle θ on the Poincaré surface. If the angular momentum L satisfies the relation $L^{-}(\theta)<L<L^{+}(\theta)$, then $(L,\theta)\in\mathcal{D}_1$, where $L^{\pm}(\theta)$ are defined by the angular momenta of the orbits that run through the points $(\mp r,0)$, respectively (see Fig. 1). More precisely, $L^{\pm}(\theta)$ are defined as

$$\begin{aligned}L^{\pm}(\theta) &= \pm r\sin(\pi-\varphi_{\pm})\\ &= \pm rR\cos\theta(R^2+r^2\mp 2Rr\sin\theta)^{-1/2},\end{aligned}\tag{1}$$

where $\varphi_{\pm}$ are defined by the angles between the horizontal axis and the orbits that run through the points $(\mp r,0)$, respectively (see Fig. 1), and given by

$$\tan\varphi_{\pm}=R\cos\theta/(-R\sin\theta\pm r).$$

Next, let us consider the domain with negative angular momentum, $L^{-}(\theta)<L<0$; the positive domain $L>0$ can be treated in the same way because of the symmetry. Solving the equation $(L^{-}(\theta))^2>L^2$ in terms of θ, the first escape domain for $L<0$ can be represented as

$$\mathcal{D}_1=\{(L,\theta)\in\mathcal{D}^{-}\,|\,\theta^{-}(L)<\theta<\theta^{+}(L)\},\tag{2}$$

where $\mathcal{D}^{-}=\{(L,\theta)\in[-r,0]\times[-\pi/2,\pi,2]\}$ is the chaotic region with negative angular momentum and $\theta^{\pm}(L)$ are defined as

$$\theta^{\pm}(L)=\arcsin\left(\frac{-L^2\pm\sqrt{L^4-L^2(R^2+r^2)+r^2R^2}}{rR}\right).\tag{3}$$

The functions $\theta^{\pm}(L)$ define the boundary of the first escape domain $\mathcal{D}_1$.

An orbit of the billiard flow starting from the first escape domain exits the cap region and stays in the stem for some time; and then it returns to the cap and reaches again to the Poincaré surface. We define the injection domain $\mathcal{D}_{\text{in}}$ on the Poincaré surface as all such just returning points, more precisely, we define $\mathcal{D}_{\text{in}}:=\Phi(\mathcal{D}_1)$. $\mathcal{D}_{\text{in}}$ can be derived in the same way as $\mathcal{D}_1$;

$$\mathcal{D}_{\text{in}}=\{(L,\theta)\in\mathcal{D}^{-}\,|\,\theta_{\text{in}}^{-}(L)<\theta<\theta_{\text{in}}^{+}(L)\},\tag{4}$$

where the functions $\theta_{\text{in}}^{\pm}(L)$ are defined by

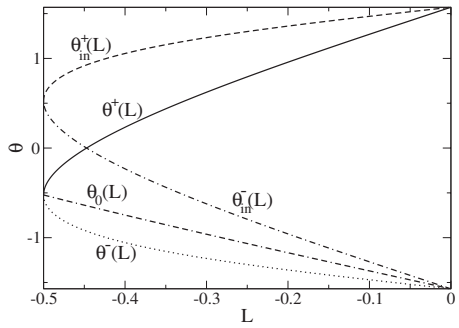

FIG. 3. The boundaries $\theta^+(L)$ (the solid line), $\theta^-(L)$ (the dotted line), $\theta^+_{\rm in}(L)$ (the dashed line), $\theta^-_{\rm in}(L)$ (the dotted-dashed line), and $\theta_0(L)$ (the dotted-two-dashed line) are displayed. We set the system parameters as $R=1$, $r=0.5$, and $h>0$. The region with negative angular momentum $L<0$ is displayed.

$$\theta^{\pm}_{\rm in}(L) = \arcsin\left(\frac{L^2 \pm \sqrt{L^4 - L^2(R^2+r^2)+r^2R^2}}{rR}\right). \quad (5)$$

In Fig. 3, $\theta^{\pm}(L)$ and $\theta^{\pm}_{\rm in}(L)$ are displayed for $R=1$, $r=0.5$ and $h>0$.

C. The inverse of the Poincaré map

When an orbit collides with the bottom of the cap

$$W := \{(x,y)|x \in [-R,-r] \cup [r,R], y=0\}, \quad (6)$$

the angular momentum changes its sign. We should take into account the collisions with this wall W, because we reduce the Poincaré map to the domain with negative angular momentum $L<0$. Let us consider the domain $\mathcal{D}^-\backslash\mathcal{D}_{\rm in}$ and its inverse image $\Phi^{-1}(\mathcal{D}^-\backslash\mathcal{D}_{\rm in})$. The orbits (namely, continuous time flow) connecting points $(L,\theta) \in \mathcal{D}^-\backslash\mathcal{D}_{\rm in}$ and $\Phi^{-1}(L,\theta) \in \Phi^{-1}(\mathcal{D}^-\backslash\mathcal{D}_{\rm in})$ are classified into two classes for fixed θ: when $L<L_0(\theta)$, there is no collision with the wall W, and when $L>L_0(\theta)$, there is a collision with the wall W [see Fig. 4(a)]. In Fig. 4(a), the orbit for the critical case $L=L_0(\theta)$ is displayed by the dashed line. We can define $L_0(\theta)$ by

$$L_0(\theta) = -R\cos(\psi-\theta), \quad (7)$$

where ψ is defined as depicted in Fig. 4(a). Furthermore, using $\tan\psi = \cos\theta/(1-\sin\theta)$, we have

$$L_0(\theta) = -R(2-2\sin\theta)^{-1/2}\cos\theta. \quad (8)$$

Solving the inequalities $L<L_0(\theta)$ and $L>L_0(\theta)$ in terms of θ, we have a result: when $\theta<\theta_0(L)$ there is no collision with the wall W, and when $\theta>\theta_0(L)$ there is a collision with the wall W, where $\theta_0(L)$ is defined by

$$\theta_0(L) = \arcsin\left(\frac{2L^2}{R^2}-1\right). \quad (9)$$

Using these results and definitions, we can construct the inverse of the Poincaré map Φ^{-1} on $\mathcal{D}^-\backslash\mathcal{D}_{\rm in}$ as follows [see Fig. 4(b)],

$$\Phi^{-1}(L,\theta) = \begin{cases} \left(L, \theta + \pi - 2\arcsin\left|\frac{L}{R}\right|\right) & \text{if } \theta < \theta_0(L), \\ \left(L, \theta - 2\arcsin\left|\frac{L}{R}\right|\right) & \text{if } \theta > \theta_0(L). \end{cases} \quad (10)$$

Notice that the angular momentum is unchanged by the collisions with the arc, and that we restrict the domain of the inverse map on the region $L<0$ by identifying the points $(-L,-\theta)$ with (L,θ) when the point particle collides with the wall W, i.e., when $\theta>\theta_0(L)$.

III. THE INFINITE PARTITION

Using the inverse map Φ^{-1}, we can define the nth escape domain $\mathcal{D}_n$ recursively:

$$\mathcal{D}_n = \Phi^{-1}(\mathcal{D}_{n-1}\backslash D_{\rm in}) \quad (n=2,3,\ldots). \quad (11)$$

Note that we should remove $\mathcal{D}_{\rm in}$ from $\mathcal{D}_{n-1}$ in the recursion relation Eq. (11), because the inverse image of the injection domain $\Phi^{-1}(\mathcal{D}_{\rm in})$ equals the first escape domain $\mathcal{D}_1$.

We fix the parameters as $R=1$, $r=0.5$ and $h>0$ in the following and explicitly derive the boundaries of the nth escape domain $\mathcal{D}_n$. First, we derive explicitly the first four escape domains in order to confirm that these four domains fill the domain $\mathcal{D}^-$ as in Fig. 5(a) except for the three regions E_1, E_2, and E_3. Then the boundary of the nth escape domain $(n \geqslant 5)$ can be derived recursively.

Let us start with $n=2$ in Eq. (11). The domain $\mathcal{D}_1/\mathcal{D}_{\rm in}$ can be divided into three pieces:

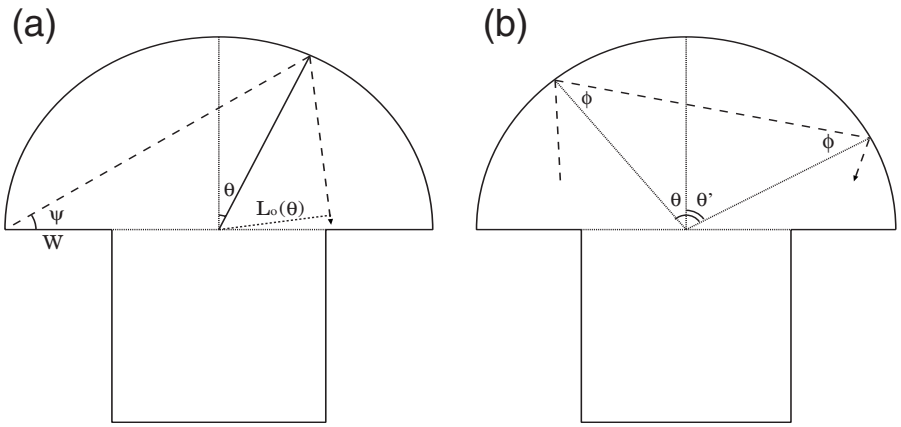

FIG. 4. (a) A classification of orbits for fixed θ: if $L_0(\theta)<L(<0)$ there is a collision with the wall W and if $L<L_0(\theta)(<0)$ there is no collision. Note that we consider only $L<0$. In the figure, we display the critical case $L=L_0(\theta)$ by the dashed line. (b) The inverse of the Poincaré map can be derived using equations $\theta=\theta'+\pi-2\phi$ and $\phi=\arcsin|L/R|$.

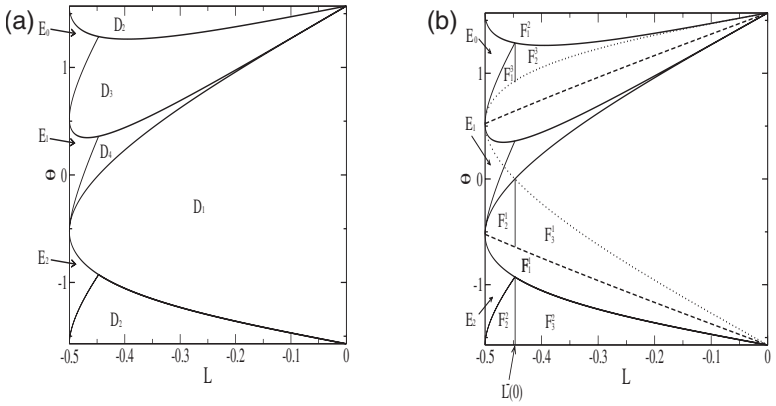

FIG. 5. (a) The first four escape domains $\mathcal{D}_1 - \mathcal{D}_4$ are displayed. The second escape domain $\mathcal{D}_2$ is separated into two parts. The remaining part consists of three pieces, which we define as E_0, E_1, and E_2. (b) The regions F_i^j are displayed. The dotted line indicates the boundary of the injection domain.

$$\mathcal{D}_1/\mathcal{D}_{\rm in} = \{(L,\theta)|\theta^-(L) < \theta < \theta_0(L)\} \cup \{(L,\theta)|\theta_0(L) < \theta < \theta^+(L), -r < L < L^-(0)\} \cup \{(L,\theta)|\theta_0(L) < \theta < \theta_{\rm in}^-(L), L^-(0) < L < 0\}, \tag{12}$$

where $L^-(0)$ is defined by Eq. (1) [see also Fig. 5(b)]. In Eq. (12), we abbreviate the expression $(L,\theta) \in \mathcal{D}^-$ to (L,θ) for simplicity. We use the same abbreviation in what follows. Let us represent the three sets on the right-hand side as $\mathcal{F}_1^1$, $\mathcal{F}_2^1$, and $\mathcal{F}_3^1$, respectively; namely, $\mathcal{D}_1/\mathcal{D}_{\rm in} = \mathcal{F}_1^1 \cup \mathcal{F}_2^1 \cup \mathcal{F}_3^1$. These three sets are displayed in Fig. 5(b). Using these notations and the inverse map Φ^{-1} [Eq. (10)], the second escape domain $\mathcal{D}_2$ is given by

$$\mathcal{D}_2 = \Phi^{-1}(\mathcal{D}_1/\mathcal{D}_{\rm in}) = \Phi^{-1}(\mathcal{F}_1^1) \cup \Phi^{-1}(\mathcal{F}_2^1) \cup \Phi^{-1}(\mathcal{F}_3^1). \tag{13}$$

Let us denote the θ component of $\Phi^{-1}(L,\theta)$ as $\Psi^L(\theta)$, and the inverse image of $\mathcal{F}_1^1$ as $\mathcal{F}_1^2 \equiv \Phi^{-1}(\mathcal{F}_1^1)$. Using these definitions, we have

$$\mathcal{F}_1^2 = \{(L,\theta)|\Psi^L(\theta^-(L)) < \theta < \Psi^L(\theta_0(L))\} = \{(L,\theta)|\theta^-(L) + \pi - 2\arcsin|L| < \theta < \pi/2)\}. \tag{14}$$

Similarly, we define the inverse image of $\mathcal{F}_2^1$ as $\mathcal{F}_2^2 \equiv \Phi^{-1}(\mathcal{F}_2^1)$, and we have

$$\mathcal{F}_2^2 = \{(L,\theta)|\Psi^L(\theta_0(L)) < \theta < \Psi^L(\theta^+(L)), -r < L < L^-(0)\} = \{(L,\theta)|-\pi/2 < \theta < \theta^+(L) - 2\arcsin|L|, -r < L < L^-(0)\}. \tag{15}$$

Finally, let us define the inverse image of $\mathcal{F}_3^1$ as $\mathcal{F}_3^2 \equiv \Phi^{-1}(\mathcal{F}_3^1)$, and we get

$$\mathcal{F}_3^2 = \{(L,\theta)|\Psi^L(\theta_0(L)) < \theta < \Psi^L(\theta_{\rm in}^-(L)), L^-(0) < L < 0\} = \{(L,\theta)|-\pi/2 < \theta < \theta^-(L), L^-(0) < L < 0\}, \tag{16}$$

where we have used the relation $\theta^-(L) - \theta_{\rm in}^-(L) = -2\arcsin|L|$. In Eq. (16), the upper bound for θ is $\theta = \theta^-(L)$, which is equivalent to the lower bound of the domain $\mathcal{D}_1$. These three sets $\{\mathcal{F}_1^2, \mathcal{F}_2^2, \mathcal{F}_3^2\}$ are displayed in Fig. 5(b).

Next, we derive the third escape domain $\mathcal{D}_3$. It can be proved that $\mathcal{D}_2 \cap \mathcal{D}_{\rm in} = \phi$, because the inequality $\theta^-(L) + \pi - 2\arcsin|L| > \theta_{\rm in}^+(L)$ holds [see the lower bound of the domain $\mathcal{F}_1^2$ which is defined by the second line of Eq. (14)]. It follows that $\mathcal{D}_3 = \Phi^{-1}(\mathcal{D}_2) = \Phi^{-1}(\mathcal{F}_1^2) \cup \Phi^{-1}(\mathcal{F}_2^2) \cup \Phi^{-1}(\mathcal{F}_3^2)$ by Eq. (11), where the three sets of the right-hand side can be calculated as

$$\Phi^{-1}(\mathcal{F}_1^2) = \{(L,\theta)|\Psi^L(\theta^-(L) + \pi - 2\arcsin|L|) < \theta < \Psi^L(\pi/2)\} = \{(L,\theta)|\theta^-(L) + \pi - 4\arcsin|L| < \theta < \pi/2 - 2\arcsin|L|\}, \tag{17}$$

and, in the same way, as

$$\Phi^{-1}(\mathcal{F}_2^2) = \{(L,\theta)|\pi/2 - 2\arcsin|L| < \theta < \theta^+(L) + \pi - 4\arcsin|L|, -r < L < L^-(0)\},$$

$$\Phi^{-1}(\mathcal{F}_3^2) = \{(L,\theta)|\pi/2 - 2\arcsin|L| < \theta < \theta^-(L) + \pi - 2\arcsin|L|, L^-(0) < L < 0\}.$$

Note that the relation $\Phi^{-1}(\mathcal{F}_1^2) \subset \mathcal{D}_{\rm in}$ holds, because of the inequalities $\theta_{\rm in}^+(L) > \frac{\pi}{2} - 2\arcsin|L|$ and $\theta^-(L) + \pi - 4\arcsin|L| > \theta_{\rm in}^-(L)$. Therefore, the fourth escape domain $\mathcal{D}_4$ is represented by $\mathcal{D}_4 = \Phi^{-1}(\mathcal{D}_3/\mathcal{D}_{\rm in}) = \Phi^{-1}(\mathcal{F}_1^3) \cup \Phi^{-1}(\mathcal{F}_2^3)$, where we define

$$\mathcal{F}_1^3 = \{(L,\theta)|\theta_{\rm in}^+(L) < \theta < \theta^+(L) + \pi - 4\arcsin|L|, -r < L < L^-(0)\}, \tag{18}$$

$$\mathcal{F}_2^3 = \{(L,\theta)|\theta_{\rm in}^+(L) < \theta < \theta^-(L) + \pi - 2\arcsin|L|, L^-(0) < L < 0\}. \tag{19}$$

These sets $\{\mathcal{F}_1^3, \mathcal{F}_2^3\}$ are displayed in Fig. 5(b). Thus, the fourth escape domain $\mathcal{D}_4$ is given by the union of the following sets:

$$\Phi^{-1}(\mathcal{F}_1^3) = \{(L,\theta)|\theta^+(L) < \theta < \theta^+(L) + \pi - 6\arcsin|L|, -r < L < L^-(0)\}, \tag{20}$$

$$\Phi^{-1}(\mathcal{F}_2^3) = \{(L,\theta)|\theta^+(L) < \theta < \theta^-(L) + \pi - 4\arcsin|L|, L^-(0) < L < 0\}, \tag{21}$$

where we have used the relation $\theta^+(L) - \theta_{\rm in}^+(L) = -2\arcsin|L|$. The lower bounds for θ of these two sets are $\theta = \theta^+(L)$; and

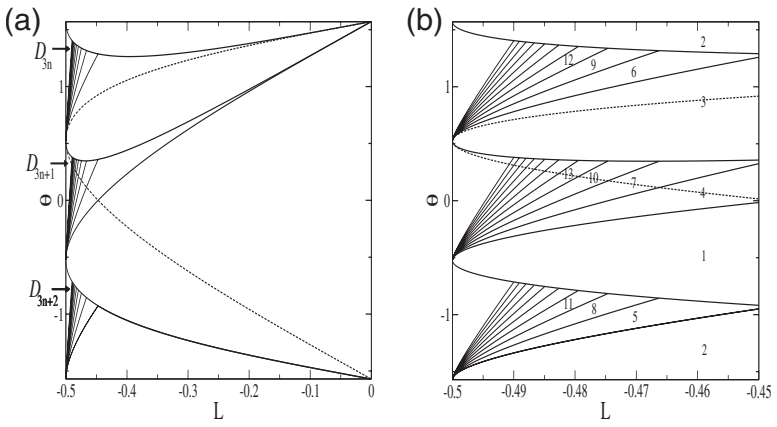

FIG. 6. (a) The infinite partition constructed in terms of the escape time. The solid lines represent boundaries between regions with different escape times. The right side of the broken line is the injection domain. The boundaries of the domains with the escape times longer than 32 are omitted. (b) A magnification of Fig. 6(a) in a neighborhood of the outermost tori ($L=-0.5$). Each number in the figure indicates the escape time of the domain where the number is located.

the upper bounds of the set $\Phi^{-1}(\mathcal{F}_2^3)$ is equivalent to the lower bound of $\mathcal{D}_3$.

From the above results, the domain $\mathcal{D}^-$ is covered by the four sets $\mathcal{D}_1$, $\mathcal{D}_2$, $\mathcal{D}_3$, and $\mathcal{D}_4$ except for the three regions E_0, E_1, and E_2 as illustrated in Figs. 5(a) and 5(b). The boundary of the nth escape domain ($n \geqslant 5$) can be obtained by recursively calculating the inverse mapping Φ^{-1} of the upper bound of the set $\Phi^{-1}(\mathcal{F}_1^3)$, which is given by Eq. (20) as $\theta = \theta^+(L) + \pi - 6\arcsin|L|$. Thus, let us define the boundary between the domains $\mathcal{D}_{3n+1}$ and $\mathcal{D}_{3(n+1)+1}$ as $\theta_{3n+1}(L)$ ($n \geqslant 1$), we have

$$\theta_{3n+1}(L) = \theta^+(L) + n\pi - 6n\arcsin|L|. \tag{22}$$

Similarly, defining the boundaries between $\mathcal{D}_{3n+2}$ and $\mathcal{D}_{3(n+1)+2}$ as $\theta_{3n+2}(L)$, and between $\mathcal{D}_{3n}$ and $\mathcal{D}_{3(n+1)}$ as $\theta_{3n}(L)$, we have

$$\theta_{3n+2}(L) = \theta^+(L) + n\pi - 2(3n+1)\arcsin|L|, \tag{23}$$

$$\theta_{3n}(L) = \theta^+(L) + n\pi - 2(3n-1)\arcsin|L|, \tag{24}$$

respectively. In Figs. 6(a) and 6(b), we depict these boundaries $\theta_n(L)$ up to $n=31$.

IV. THE ESCAPE TIME DISTRIBUTION

Finally, we derive a scaling property of the escape time distribution $f_{\rm esc}(n)$. The escape time is defined by the number of collisions with the top arc of the cap just after an orbit enters the cap region until it escapes from there.

Since the Poincaré map is area preserving, the physically natural invariant measure of the Poincaré map is the Lebesgue measure. Thus the probability that the escape time equals n is given by the Lebesgue measure $S_n^{\rm in}$ of the region $\mathcal{D}_n \cap \mathcal{D}_{\rm in}$, that is, $f_{\rm esc}(n) = S_n^{\rm in}$. Note that $S_{3n}^{\rm in} = S_{3n-1}^{\rm in} = 0$ ($n = 2,3,\ldots$), and thus only $S_{3n+1}^{\rm in}$ ($n=1,2,\ldots$) have finite values [see Figs. 6(a) and 6(b)].

Let us derive the intersection points of the lines $\theta_{3n+1}(L) = \theta^+(L) + n\pi - 6n\arcsin|L|$ [Eq. (22)] and $\theta(L)=0$. Using the Taylor expansions $\arcsin x \simeq \pm\frac{\pi}{6} + \frac{2}{\sqrt{3}}\left(x \mp \frac{1}{2}\right)$ (as $x \simeq \pm\frac{1}{2}$), we have

$$\theta_{3n+1}(L) \simeq -\frac{\pi}{6} + \frac{2}{\sqrt{3}}(3n+1)(2L+1) + \sqrt{2}(2L+1)^{1/2}, \tag{25}$$

as $n \to \infty$. Setting this to 0, and solving in terms of L, we have $2L+1 \sim \frac{1}{3n+1} \sim \frac{1}{n}$. Thus we find that the width of the $(3n+1)$-th escape domain is proportional to $1/n^2$. It follows that the area of the nth escape domain S_n behaves as

$$S_n \sim \frac{1}{n^2}, \tag{26}$$

as $n \to \infty$. Note that $S_{3n+1} = S_{3n} = S_{3n-1}$ for $n = 2,3,\ldots$, because the domains $\mathcal{D}_{3n}$ and $\mathcal{D}_{3n-1}$ have no intersection with the domain $\mathcal{D}_{\rm in}$. Equation (26) shows that the partition constructed in the previous section is infinite. Finally, we get

$$S_{3n+1}^{\rm in} = S_{3n+1} - S_{3n+4} \sim \frac{1}{n^3}, \tag{27}$$

as $n \to \infty$. And, as mentioned above, the equalities $S_{3n}^{\rm in} = S_{3n-1}^{\rm in} = 0$ hold. This power law perfectly agrees with the numerical result shown in Fig. 7, where the cumulative distribution

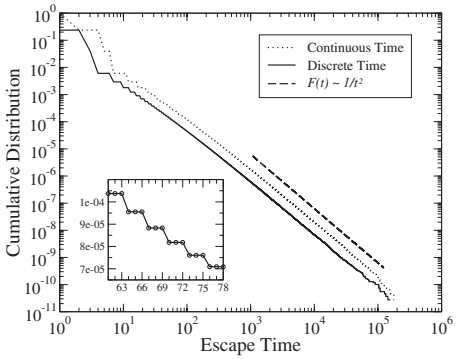

FIG. 7. The cumulative distributions of the escape time for the discrete time case (the solid line) and for the continuous time case (the dotted line) in log-log scale. The dashed line is the analytical result $F(t) \sim 1/t^2$. The inset is a magnification of the discrete time case, which shows a clear stepwise structure.

$$F_{\mathrm{esc}}(n) \coloneqq \sum_{j=n+1}^{\infty} f_{\mathrm{esc}}(j) \tag{28}$$

is displayed by the solid line. Note that this numerical result has already been reported by Altmann *et al.* [20]. In the inset, a magnification is displayed, which shows a clear stepwise structure with decreases exactly at $n=3k+1$ $(k=1,2,\ldots)$. This implies that $f_{\mathrm{esc}}(3k)=f_{\mathrm{esc}}(3k+2)=0$, and that the only $f_{\mathrm{esc}}(3k+1)$ have finite values $(k \geqslant 2)$. Thus, these results also agree with the analytical results.

V. CONCLUDING REMARKS

In conclusion, we have derived the escape time distribution by constructing the infinite partition in terms of the escape time. Note that, however, the escape "time" in this paper is the number of collisions until the particle escapes. Thus the escape time for the continuous time flow might be slightly different. But the scaling exponents should be the same, because the flight time of the chaotic orbits between collisions in the cap region is nonvanishing. This is confirmed numerically and the result is displayed in Fig. 7 which shows the agreement of the scaling exponents of these two distributions.

There are several points that should be verified in future studies. First, the correlation functions of this system exhibit power law behaviors (Fig. 8, see also, Ref. [17]), and it is expected that there is a relation between the scaling exponent of the escape time distribution and that of the correlation function [16]. Second, it is important to elucidate whether the results in this paper are general or not for other parameter values $R \neq 2r$. Third, it is also important to consider how general the results of the present paper are in Hamiltonian systems. Especially, it is necessary to investigate systems with 3 and more degrees of freedom (DOF), because the mushroom billiard is a system with 2 DOF, while systems with 3 and more DOF differ qualitatively from systems with 2 DOF by the presence of Arnold diffusion [4].

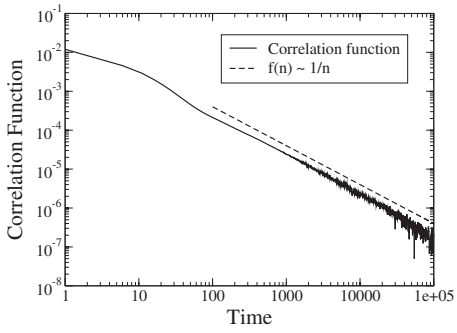

FIG. 8. The autocorrelation function of the absolute value of the angular momentum $|L|-\langle|L|\rangle$ (the solid line) in log-log scale, where $\langle\cdots\rangle$ means the ensemble average in terms of the Lebesgue measure in the chaotic domain. The broken line represents a function $f(n) \sim 1/n$, which is a guide to the eye.

ACKNOWLEDGMENTS

The author would like to thank Y. Aizawa and A. Shudo for valuable discussions and comments, and E. G. Altmann for drawing his attention to Ref. [21]. This work was supported in part by Waseda University Grant for Special Research Projects (the Individual Research Grant No. 2005B-243) from Waseda University.

[1] D. Ruelle, Phys. Rev. Lett. **56**, 405 (1986).
[2] P. Gaspard, *Chaos, Scattering and Statistical Mechanics* (Cambridge University Press, Cambridge, 1998).
[3] J. R. Dorfman, *An Introduction to Chaos in Non-equilibrium Statistical Mechanics* (Cambridge University Press, Cambridge, 1999).
[4] A. J. Lichtenberg and M. A. Lieberman, *Regular and Chaotic Dynamics*, 2nd ed. (Springer-Verlag, Berlin, 1992).
[5] C. F. F. Karney, Physica D **8**, 360 (1983).
[6] R. S. Mackay, J. D. Meiss, and I. C. Percival, Physica D **13**, 55 (1984).
[7] B. V. Chirikov and D. L. Shepelyansky, Physica D **13**, 395 (1984).
[8] T. Geisel, A. Zacherl, and G. Radons, Phys. Rev. Lett. **59**, 2503 (1987).
[9] T. H. Solomon, E. R. Weeks, and H. L. Swinney, Phys. Rev. Lett. **71**, 3975 (1993).
[10] P. Manneville and Y. Pomeau, Phys. Lett. **75A**, 1 (1979).
[11] Y. Pomeau and P. Manneville, Commun. Math. Phys. **74**, 189 (1980).
[12] T. Geisel and S. Thomae, Phys. Rev. Lett. **52**, 1936 (1984).
[13] Y. Aizawa, Y. Kikuchi, T. Harayama, K. Yamamoto, M. Ota, and K. Tanaka, Prog. Theor. Phys. Suppl. **98**, 36 (1989).
[14] S. Tasaki and P. Gaspard, J. Stat. Phys. **109**, 803 (2002).
[15] R. Artuso and G. Cristadoro, J. Phys. A **37**, 85 (2004).
[16] T. Miyaguchi and Y. Aizawa, e-print arXiv:nlin.CD/0702032 (unpublished).
[17] L. A. Bunimovich, Chaos **11**, 802 (2001).
[18] J. Malovrh and T. Prosen, J. Phys. A **35**, 2483 (2002).
[19] L. A. Bunimovich, Chaos **13**, 903 (2003).
[20] E. G. Altmann, A. E. Motter, and H. Kantz, Chaos **15**, 033105 (2005).
[21] E. G. Altmann, A. E. Motter, and H. Kantz, Phys. Rev. E **73**, 026207 (2006).
[22] H. Tanaka and A. Shudo, Phys. Rev. E **74**, 036211 (2006).
[23] B. Dietz, T. Friedrich, M. Miski-Oglu, A. Richter, T. H. Seligman, and K. Zapfe, Phys. Rev. E **74**, 056207 (2006).
[24] M. J. Davis and S. K. Gray, J. Chem. Phys. **84**, 5389 (1986).
[25] H. Waalkens, A. Burbanks, and S. Wiggins, Phys. Rev. Lett. **95**, 084301 (2005).
[26] C. Jaffé, D. Farrelly, and T. Uzer, Phys. Rev. Lett. **84**, 610 (2000).
[27] D. Beigie, A. Leonard, and S. Wiggins, Chaos, Solitons Fractals **4**, 749 (1994).